

See discussions, stats, and author profiles for this publication at: <https://www.researchgate.net/publication/231645385>

# Electrochemical Nucleation and Growth of Gold Nanoparticles on Single-Walled Carbon Nanotubes: New Mechanistic Insights

ARTICLE *in* THE JOURNAL OF PHYSICAL CHEMISTRY C · JULY 2010

Impact Factor: 4.77 · DOI: 10.1021/jp1043706

---

CITATIONS

41

---

READS

20

3 AUTHORS, INCLUDING:



**Julie V Macpherson**

The University of Warwick

**175** PUBLICATIONS **5,518** CITATIONS

SEE PROFILE

# Electrochemical Nucleation and Growth of Gold Nanoparticles on Single-Walled Carbon Nanotubes: New Mechanistic Insights

Petr V. Dudin, Patrick R. Unwin,\* and Julie V. Macpherson\*

Department of Chemistry, University of Warwick, Coventry, United Kingdom, CV4 7AL

Received: May 13, 2010; Revised Manuscript Received: June 22, 2010

The electrodeposition mechanism of gold nanoparticles (NPs) on pristine single walled carbon nanotubes (SWNTs) at high driving forces has been elucidated using the microcapillary electrochemical method. Here, a small capillary (internal diameter  $\sim 50\text{--}100\ \mu\text{m}$ ) filled with a gold plating solution, and positioned so that the capillary meniscus makes contact with a two-dimensional SWNT random network, was used to record current–time transients. Nucleation and growth transients were observed in which the current increased with time to a maximum value beyond which the current decreased (planar diffusion regime). With increased driving force, the current maximum shifted dramatically to increasingly shorter times. Atomic force microscopy (AFM) analysis indicated that this was not due to significant differences in NP growth rates, but rather to increased densities of NPs formed at more cathodic potentials. Detailed microscopic analysis showed that the size of the NPs initially increased with deposition time and the particle surface coverage was constant. However, at the highest driving forces the NP density decreased with deposition time and AFM revealed the presence of both larger and smaller particles at long times. This was attributed to electrochemically induced Ostwald ripening, whereby larger particles grow at the expense of smaller ones. As NP nucleation and growth on SWNT two dimensional network electrodes is highly directional and enforced in particular locations, it is inappropriate to analyze electrochemical data using conventional models. There is thus a need to complement chronoamperometric measurements with high resolution microscopy to fully interpret nucleation on complex electrode surfaces.

## Introduction

Carbon nanotubes (CNTs) have attracted tremendous interest due to their promising physical and chemical properties.<sup>1,2</sup> In the electrochemical arena, their high intrinsic electrical conductivity<sup>3</sup> coupled with their nanoscopic dimensions mean that CNTs can function as nanoscale conducting wires and electrodes. As such, they have been used extensively for a variety of electrochemical applications.<sup>4–7</sup>

The electrochemical properties of CNTs can be further extended by combination with nanoparticles (NPs); particularly as NPs can bestow enhanced electrocatalytic activity.<sup>8</sup> Electrodeposition is a particularly attractive route to forming NP structures since through choice of substrate, deposition potential, and growth time, it is possible to direct the nucleation process toward either nanoparticle or nanowire growth.<sup>9</sup> Furthermore, it is possible to analyze the current–voltage–time response of the electrodeposition process to provide key mechanistic information.<sup>10–14</sup> Electrodeposition has been exploited to produce CNT-NP structures of varying NP density and sizes, ranging from isolated nanoparticles to contiguous nanowires.<sup>15,16</sup>

There has been much interest in using single walled carbon nanotubes (SWNTs) for the controlled electrodeposition of NPs, due to their very small diameter (typically 1–3 nm). The 1D nature of a SWNT also provides an ideal template for electrodeposition, especially to gain directional control over NP position. Using this methodology, the electrodeposited NPs are “pristine” or “naked”, making direct contact with the underlying CNT and providing efficient electron transport pathways from CNT to NP. This contrasts with synthetic routes, where

chemically preformed metal NPs are typically ligand-stabilized to prevent agglomeration,<sup>17–19</sup> and then deposited in this form onto CNTs.

SWNTs have been employed as a scaffold for direct electrodeposition of several metals, which are known electrocatalysts, including Ag,<sup>15,20–24</sup> Pt,<sup>15,25,26</sup> Pd,<sup>26,27</sup> Au,<sup>16</sup> Ni<sup>28</sup> and Cu.<sup>19</sup> To date, however, there have been relatively few studies<sup>26,28</sup> exploring the electronucleation and growth mechanism of metals on SWNTs.

Gold NPs represent the first known colloidal system.<sup>29</sup> Although for many years they were considered “chemically inert and uninteresting”,<sup>30</sup> In recent decades it has been shown that Au NPs are catalytically active toward numerous electrochemical processes, such as glucose oxidation,<sup>31</sup> oxygen and hydrogen peroxide reduction,<sup>32</sup> and the reduction of sulfur.<sup>33</sup> In order to optimize catalytic system based on Au NPs-SWNTs, it is essential that the electrodeposition mechanism of Au NPs on SWNTs is understood in detail, in order to produce structures with defined Au NP sizes and spacing.

In this work, we present a comprehensive study of Au NP nucleation at high driving force on two-dimensional planar networks of SWNTs (surface coverage <1%) supported on an insulating surface, using the microcapillary electrochemical method (MCEM) in conjunction with high resolution microscopy characterization.<sup>26</sup> In MCEM, the solution of interest is confined within a glass microcapillary (internal diameter <100  $\mu\text{m}$ ), which also contains a reference electrode. The substrate, comprising the SWNT network,<sup>34–36</sup> functions as the working electrode. This simple approach (i) negates the use of lithographic processing of the SWNT sample; (ii) enables many electrodeposition measurements to be taken in short periods of

\* To whom correspondence should be addressed. E-mail: p.r.unwin@warwick.ac.uk; j.macpherson@warwick.ac.uk.

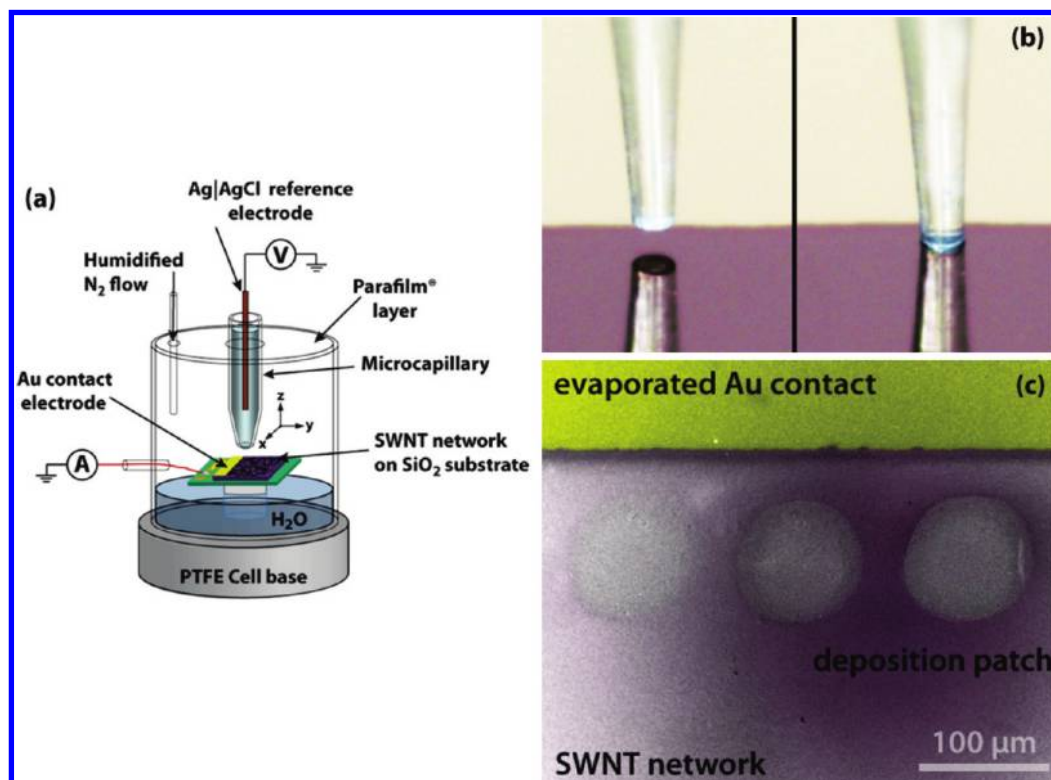


**Figure 1.** (a) Schematic of the microcapillary arrangement. (b) Movement of the solution-filled microcapillary (90  $\mu\text{m}$  inner diameter) toward the SWNT-SiO<sub>2</sub> surface; the reflection of the capillary is clearly visible. Right hand side: contact between the solution contained within the capillary and the substrate; note the capillary does not touch the surface. (c) FE-SEM image of the SWNT sample after Au deposition in three locations using the MCEM. The contact area of the solution filled capillary and substrate is clearly visible and contrasts with the surrounding SWNT-SiO<sub>2</sub> substrate.

time on one sample, simply by moving the position of the capillary to a new location, and (iii) allows measurements on relatively fast time scales.

### Experimental Section

**SWNT Growth.** SWNT synthesis has been described previously in detail.<sup>37</sup> In general, SWNTs were grown on insulating Si/SiO<sub>2</sub> substrates (300 nm of thermally grown oxide) by catalyzed chemical vapor deposition (cCVD), using iron nanoparticles as the catalyst. The catalyst was formed from a submonolayer film of ferritin, from which the protein shell was removed using an oxygen plasma. Methane was employed as the carbon-containing feedstock gas. Growth conditions were selected<sup>35</sup> which yielded random two-dimensional networks of SWNTs with an average nanotube density of  $\sim 4 \mu\text{m}$  length of SWNT per  $\mu\text{m}^2$  area of the supported substrate. This is above the percolation threshold of metallic SWNTs,<sup>35</sup> ensuring there are continuous metal-metal-SWNTs contacts throughout the network, but with a surface coverage of less than 1% of the underlying insulating surface.<sup>37</sup>

**SWNT Electrode Fabrication.** A gold band providing electrical contact to the SWNT network, was thermally evaporated (Au 100 nm with a Cr adhesive layer 2 nm) using a shadow mask.

**Solutions.** Gold deposition solutions consisted of Milli-Q reagent water (Millipore Corp., 18 M $\Omega$  cm) containing 1 mM KAuCl<sub>4</sub> (99.999%, Aldrich) with 0.2 M KNO<sub>3</sub> (Fisher Scientific).

**Microcapillary Set Up.** All electrochemical measurements were carried out using a microcapillary electrochemical cell, as previously described<sup>26</sup> and shown schematically in Figure 1(a). Borosilicate glass capillaries (1.2 mm outer diameter, 0.69

mm internal diameter, Harvard Apparatus Ltd.) were pulled to a fine point using a laser pipet puller (model P-2000, Sutter Instrument Co.) and then polished flat, using a home-built polishing setup, where the capillary was held vertical with respect to the polishing disk (0.5  $\mu\text{m}$  polishing pad, Buehler). Typically, capillaries with internal diameters of  $\sim 50$ – $100 \mu\text{m}$  were employed.

Prior to use, the outer wall of the microcapillary was silanized by connecting it to an internal flow of N<sub>2</sub> (to protect the inside from silanization) and immersing the end into dimethyldichlorosilane (Fisher Scientific) for  $\sim 2$  min. The SWNT substrate was mounted inside a humidity cell as shown in Figure 1(a), and the Au band connecting the SWNTs, was bonded with a gold wire.

Approach of the microcapillary to the surface of interest was performed using a manually controlled *x-y-z* micropositioner (Newport: resolution 1  $\mu\text{m}$ ); aided by optical visualization from a USB camera (PixelINK, Edmund Optics). As shown in Figure 1(b), the reflection of the microcapillary in the SiO<sub>2</sub>–SWNT surface was utilized to position the probe in the plane of the surface. The microcapillary was then translated toward the SWNT/SiO<sub>2</sub> surface until the meniscus was seen to wet the surface (Figure 1(b)). In this way, the capillary itself never makes contact with the substrate.

The humidity controlled environment and capillary silanization helped to prevent evaporation of solution from the capillary and yielded a well-defined contact area of the solution with the SWNT network. This is verified in the optical micrograph of Figure 1(c), which shows electrodeposition patches after a series of experiments, using the same capillary. Typically, discs 50–100  $\mu\text{m}$  in diameter resulted (dependent on the inner

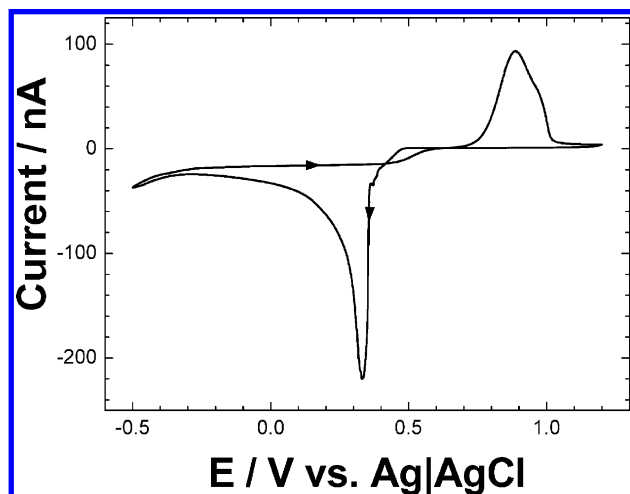


**Figure 2.** CV for the electrodeposition and oxidation of Au on a SWNT network from a solution containing 1 mM KAuCl<sub>4</sub> and 0.2 M KNO<sub>3</sub>, at a scan rate of 100 mV s<sup>-1</sup>, using a microcapillary of internal diameter 53  $\mu$ m.

diameter of the microcapillary utilized); the dimensions of which were verified after experiments by optical and electron microscopy.

The entire set up was shielded with a Faraday cage and mounted on a home-built marble bench, incorporating vibration isolators.

**Electrodeposition of Au NPs.** Au NPs were deposited using both chronoamperometry and cyclic voltammetry (CV), in the microcapillary cell, with a two-electrode arrangement. A freshly prepared quasi-reference Ag|AgCl electrode (chloridised 250  $\mu$ m diameter Ag wire<sup>38</sup>) was placed inside the capillary, with the SWNT network functioning as the working electrode. All the potentials reported in the work are quoted against the Ag|AgCl electrode. Note that there was no noticeable interference from the release of silver ions on the time scale of the measurements. The potential of the Ag|AgCl wire in the plating solution was measured against the saturated calomel electrode, in the same solution, and found to differ by  $\pm 2$  mV. All measurements were made with a CH Instruments Model 600B (Austin, TX) potentiostat and with the microcapillary typically placed about 50–100  $\mu$ m from the Au-band contact (Figure 1(d)), so that resistive effects from the SWNT network were negligible. After each Au electrodeposition chronoamperometric experiment, the potential of the SWNT electrode was returned to +0.75 V for a period of ca. 10 s before removal of the capillary.

**High Resolution Microscopy.** Atomic Force Microscopy (AFM) images were taken in tapping mode using a Veeco Multimode AFM (with a Nanoscope IIIa controller Extender module). SPIP software (Image Metrology) was employed for analysis of the Au NP heights. Field emission - scanning electron microscopy (FE-SEM) images were acquired using a SUPRA 55 variable pressure system (Zeiss).

## Results and Discussion

**Electrochemical Studies.** Figure 2 shows a typical CV for the electrodeposition of Au onto a two-dimensional planar SWNT network electrode. The capillary employed had an inner diameter of 53  $\mu$ m and contained 1 mM KAuCl<sub>4</sub> in 0.2 M KNO<sub>3</sub> (pH 5). The CV was recorded at a potential scan rate of 100 mV s<sup>-1</sup>, commencing at +0.75 V with an initial sweep negative to -0.5 V, positive again to +1.2 V and then back to +0.75 V.

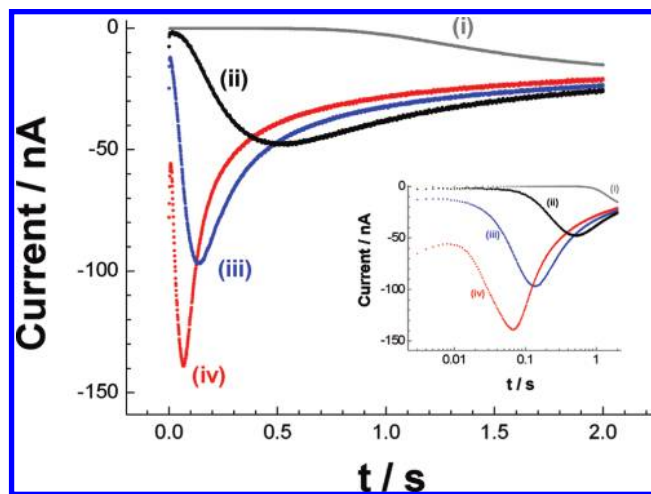
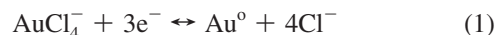


**Figure 3.** Current–time transients recorded for Au electrodeposition on a two-dimensional SWNT network electrode using a microcapillary of internal diameter 82  $\mu$ m at potentials of (i) +300 mV (gray line), (ii) +200 mV (black line), (iii) 0 mV (blue line), and (iv) -200 mV (red line). Inset: the same transients plotted with logarithmic time to emphasize the short time behavior.

The CV shown is typical for Au electrodeposition on carbon-based electrodes,<sup>39,40</sup> where the cathodic peak (on the first scan) at ca. +0.32 V is due to reduction of AuCl<sub>4</sub><sup>-</sup> to Au (eq 1), which becomes apparently diffusion-limited at more cathodic potentials and longer times. The current flow at ca. -0.35 V is associated with the onset of catalytic O<sub>2</sub> reduction on the electrodeposited gold nanostructures.<sup>41</sup>

On the anodic-going scan, the peak at ca. +0.9 V, with a shoulder at +1.0 V, is likely to be due to surface oxidation of the electrodeposited gold.<sup>39,42–44</sup> However, we cannot rule out completely a possible contribution from the dissolution (electro-oxidation) of gold, which is especially favorable in a Cl<sup>-</sup> environment (eq 1).<sup>42</sup>



From knowledge obtained from the CV measurements (Figure 2), chronoamperometry was employed to investigate further gold electrodeposition on the SWNTs. High driving forces, more cathodic than the cathodic peak in Figure 2 were considered, but deposition potentials were chosen to avoid current contributions from unwanted side processes, e.g., H<sub>2</sub> evolution or O<sub>2</sub> reduction. Typical current (*i*) – time (*t*) transients are depicted in Figure 3. Here, the potential has been stepped from +0.75 V, where no faradaic processes occur, to successively more negative driving potentials, +0.3 V (i); +0.2 V (ii); 0 V (iii); and -0.2 V (iv), each for a time period of 2 s. Each measurement was made in a new location on the SWNT surface (e.g., as shown in Figure 1(c)).

For each of the traces in Figure 3, the initial increase in current with time is ascribed to Au particle nucleation and growth.<sup>45</sup> After an initial charging current at very short times (where the current decreases with time), the current increases, reaches a peak and then decreases indicating complete overlap of all of the diffusion fields of the growing particles. The peak current, as shown in Figure 3, shifts to shorter time scales as the driving potential is made more negative, and nucleation is favored, i.e., +300 mV (no peak reached after 2 s); +200 mV (peak at 0.5 s); 0 mV (peak at 0.13 s); -200 mV (peak at 0.06 s). This is further emphasized in the inset to Figure 3 which shows



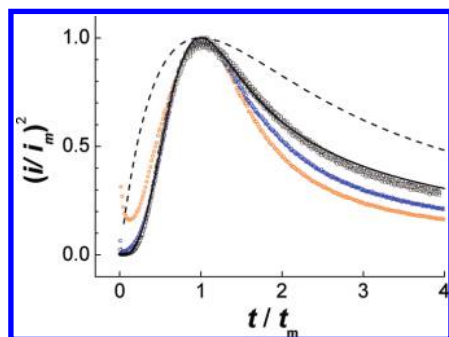


**Figure 4.** Nondimensional  $(i/i_m)^2$  vs  $(t/t_m)$  plots of the data in Figure 3, for +200 mV (black circles), 0 mV (blue circles), -200 mV (red circles), together with the theoretical curves for progressive nucleation (black solid line) and instantaneous nucleation (dashed black line), as described by the SH model.

the same transients plotted as logarithmic time to emphasize the short time behavior.

The most widely used method to model the nucleation and growth of metal particles from experimental  $i-t$  transients was developed by Scharifker and Hills<sup>45</sup> (SH model), from which other models have stemmed,<sup>46,47</sup> but which are all based on the Johnson–Mehl–Avrami–Kolmogorov (JMAK) theorem.<sup>48–53</sup> The SH model gives expressions for  $i$  as a function of  $t$ , for the limiting cases of instantaneous and progressive nucleation, although it should be noted that the concept of truly instantaneous growth has been debated in detail elsewhere.<sup>11–14,54,55</sup> The SH model does not take into account induction times associated with nucleation, which are clearly evident in the data shown in the inset to Figure 3.

The  $i-t$  data (Figure 3) for deposition at +200 mV, 0 V, and -200 mV, was fitted to the SH model, where the data is plotted in dimensionless coordinates  $(i/i_m)^2$  vs  $t/t_m$ .  $i_m$  and  $t_m$  represent the maximum peak current of the recorded  $i-t$  transient and the corresponding time, respectively. Equations 2 and 3 express the case of instantaneous and progressive nucleation in the SH model (Figure 4).<sup>45</sup>

$$\left(\frac{i}{i_m}\right)_{\text{inst.}}^2 = 1.9542 \left(\frac{t_m}{t}\right) \left\{ 1 - \exp \left[ -1.2564 \left(\frac{t}{t_m}\right) \right] \right\}^2 \quad (2)$$

$$\left(\frac{i}{i_m}\right)_{\text{progr.}}^2 = 1.2254 \left(\frac{t_m}{t}\right) \left\{ 1 - \exp \left[ -2.3367 \left(\frac{t}{t_m}\right)^2 \right] \right\}^2 \quad (3)$$

Dimensionless representation of the  $i-t$  transient usually indicates the particular nucleation type and does not contain quantities such as nuclei number (density) or rate of nucleation and overpotential.

For the case of deposition at +200 mV (black open circles) close agreement with the theory for progressive nucleation is observed. In general, for all deposition potentials, nucleation resembles more closely progressive growth than instantaneous, although as the driving potential is made more negative, the current is observed to decay (once past the current maxima) faster than predicted by theory.

It is well documented that the SH model has proven to be a good description for metal nucleation processes occurring on conventional carbon metal and semiconductor electrodes (e.g., as described in refs 39, 56–61). However, for the case of the very low surface coverage SWNT network electrode we cannot

assume random nucleation, which is a postulate of the JMAK theorem, as nucleation and growth is forced along certain directions by the SWNT network. As we highlight further below, it is thus essential that the chronoamperometric studies are undertaken in conjunction with high resolution microscopic analysis of the resulting surface, to correctly interpret the experimental  $i-t$  behavior.

**High Resolution Microscopy Studies.** AFM and FE-SEM imaging and analysis were performed after chronoamperometric electrodeposition using the MCEM at different driving potentials ( $V_{\text{dep}}$ ) for different time periods. Each electrodeposition, for a defined  $V_{\text{dep}}$  and time period, was carried out five times, in different areas of the random network (but at the same distance from the Au band) in order to obtain representative information.

Typical tapping mode AFM height images,  $3 \times 3 \mu\text{m}$ , of the resulting Au-SWNT structures are shown in Figure 5 after electrodeposition at: (a) +200 mV; (b) 0 mV and (c) -200 mV for (i) 0.1 s, (ii) 0.5 s, (iii) 2 s, and (iv) 5 s. In all AFM images, it is possible to clearly identify the Au NPs which electronucleate *only* on the sidewalls of the SWNTs. Also observed (at the shortest time scales where the AFM height scale is the smallest) are very small unreacted catalyst particles (typical heights 4–7 nm) that sit on the  $\text{SiO}_2$  surface and are unconnected to the SWNTs. They thus play no role in the electrochemical process. We did not observe spontaneous electroless deposition of  $\text{Au}^0$  on the unbiased surface (as reported by some authors<sup>62</sup>) even after the sample was left in the electrolyte solution for 48 h.

The NP height distribution for each deposition potential and time is plotted in histogram form under each AFM image. Note, in the case of  $V_{\text{dep}}$  at +200 mV and 0 mV, the NP particle size distribution was calculated from larger  $8 \mu\text{m} \times 8 \mu\text{m}$  scans, in order to obtain sufficient NP numbers to enable a statistical analysis. It can be seen clearly that for all driving potentials, the size of the NPs produced increased as the deposition time increased (from 0.1 to 5 s), with the largest particles being produced at the lower driving forces (more positive potentials) and longest times. For example, from the histogram data, at +200 mV (Figure 5(a)) the particles grow in height from  $15.0 \pm 4.8$  (s.d) nm (Figure 5(ai)) at 0.1 s to  $68.0 \pm 25.1$  (s.d) nm (Figure 5(aiv)), after 5 s. At 0 mV the height change is  $16.7 \pm 4.0$  (s.d) nm at 0.1 s (Figure 5(bi)) to  $57.8 \pm 13.0$  (s.d) nm after 5 s (Figure 5(biv)). After 5 s, at all of the deposition potentials, the size distribution is also widest with both small and large particles being observed on the SWNTs; this is especially prominent at a  $V_{\text{dep}}$  of -200 mV.

To obtain information on particle number densities, FE-SEM was employed (typical data shown in Supporting Information) as it could be used to image the surface faster and over larger areas than AFM (although FE-SEM could not provide quantitative data on particle size due to charging effects). Figure 6 summarizes data for the Au NP number density, calculated from three  $12 \times 8 \mu\text{m}$  FE-SEM images for the same deposition times and potentials as shown in Figure 5. It can be seen that the number density is much larger for deposition at -200 mV, compared to either 0 mV or +200 mV. Moreover, at the lower driving forces of 0 mV and +200 mV, the number of NPs is observed to stay relatively constant with time, in the range 1–4 NPs  $\mu\text{m}^{-2}$ . However, at -200 mV the number of particles decreases with increasing electrodeposition time from  $40.1 \pm 2.5$  NPs  $\mu\text{m}^{-2}$  to  $17.0 \pm 3.0$  NPs  $\mu\text{m}^{-2}$ .

From the integrated charge, passed during chronoamperometric deposition, and knowing the particle density (as measured in Figure 6) the “average” NP size (for a given  $V_{\text{dep}}$  and deposition time) can be calculated and compared to the images

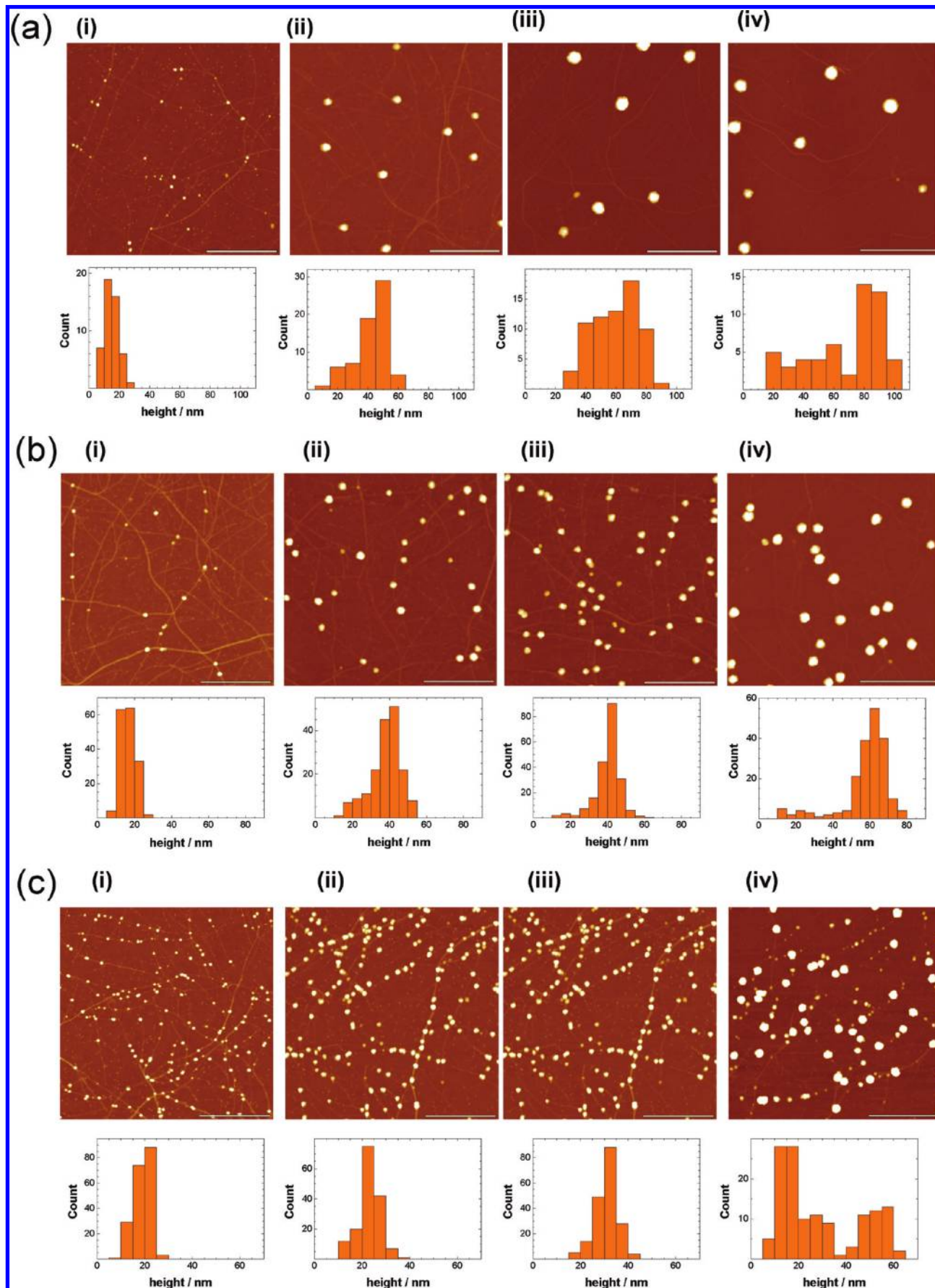


**Figure 5.** Representative AFM height images,  $3 \times 3 \mu\text{m}$ , recorded for MCEM gold deposition from a solution containing 1 mM KAuCl<sub>4</sub> and 0.2 M KNO<sub>3</sub> at: (a) +200 mV; (b) 0 mV and (c) -200 mV for time periods of (i) 0.1 s; (ii) 0.5 s; (iii) 2 s and (iv) 5 s. Histogram of NP height distribution, underneath each image, were taken from larger  $8 \times 8 \mu\text{m}$  AFM images (and from  $3 \times 3 \mu\text{m}$  images for -200 mV) recorded in the same area. The scale bar in all cases represents 1  $\mu\text{m}$ .

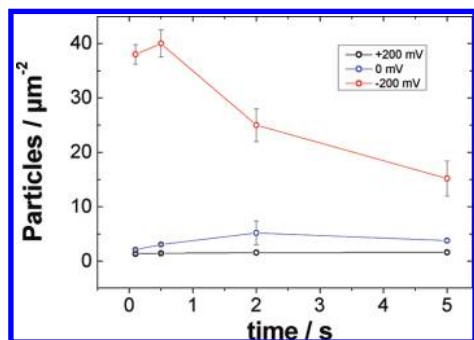


**Figure 6.** Plot of NP number density (as particles per  $\mu\text{m}^2$ ) as a function of deposition time, for three different deposition potentials: +200 mV (black open circles); 0 mV (blue open circles) and -200 mV (red open circles).

shown in Figure 5. Making the assumption that the NPs are spheres, the mean particle size is given by the following:<sup>63</sup>

$$r = \left( \frac{3QM}{4\pi nF\rho} \right)^{1/3} \quad (4)$$

where  $r$  is the radius of the sphere,  $Q$  is the charge passed per particle (derived by relating the integral charge from the  $i-t$  transient to NP density and electrochemical contact area, measured by FE-SEM),  $M$  and  $\rho$  are the molar mass and density of the Au NP particle, 196.97 g mol<sup>-1</sup> and 19.30 g cm<sup>-3</sup>, respectively,  $n$  ( $= 3$ ) is the number of electrons passed for the discharge of Au (eq 1) and  $F$  is the Faraday constant (96 485 C mol<sup>-1</sup>). The calculated mean particle sizes are given in Table 1, along with the measured values from AFM images. As can be seen, the calculated mean NP sizes correlate quite well with those obtained from the AFM data, except at the longest time scales (vide infra) indicating that the microscopic analysis is a reflection of the electrodeposited structures.

Significantly, the AFM and FE-SEM data contradict the nucleation and growth mechanism evaluated using the SH model from  $i-t$  transient analysis alone. In fact, microscopy analysis clearly shows that at +300 mV (data not shown), +200 mV and 0 mV the number of nuclei/particles is fairly fixed with time (Figure 6). In this regime NPs simply get larger with time. In contrast, at a driving force of -200 mV, and after 0.5 s, the particle number density decreases with time.

Although for many electrochemical processes and time scales the area of the SWNT network electrode is controlled by the wetting of the microcapillary meniscus on the substrate,<sup>23,37</sup> the actual surface coverage of the SWNTs network is below 1% of this geometric area<sup>35</sup> and metal deposition is thus restricted to defined regions only, i.e., only the SWNT network. Thus, with this electrode arrangement there are three time-dependent diffusional regimes to consider during NP nucleation and growth, as shown schematically in Figure 7.

(1) At very short times neighboring diffusion fields from nucleated and growing particles are isolated;<sup>64</sup>

(2) with time, these fields merge and diffusion to individual SWNTs dominates. Finally, with further increase in time,<sup>65</sup>

(3) the diffusion profiles of individual SWNTs overlap and planar diffusion to the entire geometric area results. For electrodeposition at conventional electrode surfaces only diffusion regimes (1) and (3) operate.

Figures 5 and 6 also evidence that at the highest driving force (-200 mV) there are many more nucleation sites on the SWNT sidewall. Similar observations were made for Pd electrodeposition on SWNT network electrodes.<sup>26</sup> We attribute this to the large electrochemical overpotential, which promotes nucleation over the entire sidewall (not just at energetically favorable defect sites) and acts to suppress any apparent differences in electrochemical behavior between semiconducting and metallic SWNTs.<sup>26,66</sup>

Similar NP sizes are found at 0.1 s at different driving forces (Table 1 and Figure 5, parts (ai), (bi), and (ci)). This suggests that within the potential range investigated, the overpotential has no apparent significant effect on the initial rate of growth of the nuclei. Thus, the clearly different growth transients in Figure 3 (notably at short times) are essentially a consequence of different NP surface coverages.

Of particular interest is the observation that at long times ( $>2$  s), for all driving potentials, the occurrence of both larger and smaller particles is more prominent, especially at the highest driving force (-200 mV) where there is an almost bimodal distribution of particle sizes (Figure 5(civ)). We believe it is unlikely that there is a time-dependent switch in nucleation mechanism from "instantaneous" to "progressive". Indeed, given our careful analysis, this can be ruled out, because the coverage of NP decreases with time. Instead, we attribute this observation to Ostwald ripening, where larger clusters grow at the expense of smaller ones. Typically, Ostwald ripening is known to be a very slow process<sup>67</sup> which can take days,<sup>68</sup> however electrochemically facilitated surface diffusion and mass redistribution has been reported to occur within the time scale of an electrochemical experiment (ranging from milliseconds<sup>69</sup> to tens of seconds<sup>70</sup>).

The nonuniform particle size distribution is significant under conditions where the particles are more closely spaced on the supporting SWNTs. Slightly smaller particles with larger surface energies are energetically less stable than the larger ones, thus with time the larger ones grow at the expense of the smaller ones which dissolve to feed this growth. This process naturally involves significant interaction between neighboring NPs, facilitated by both the overlapping (interacting) diffusion fields of individual NPs and the underlying SWNTs which provide a conducting support (Figure 8). This explains why we see this effect more dramatically for Au NPs which grow with the highest nucleation density (i.e., most closely spaced).

It is also important to note that density functional theory calculations show Au clusters to be very mobile on SWNT sidewalls,<sup>71</sup> which could also be a contributing factor in the Ostwald ripening observed here. Finally, the local dissolution of smaller Au NPs is likely to be further promoted by the release

**TABLE 1: Experimentally Measured Au NP Heights (in nm) and Calculated Au NP Heights (bracketed bold text) for Different Deposition Potentials and Times Using the MCEM**

deposition potential	deposition time/s			
	0.1	0.5	2.0	5.0
+200 mV	15.0 $\pm$ 4.8 ( <b>16.6 <math>\pm</math> 0.9</b> )	42.7 $\pm$ 10.3 ( <b>44.1 <math>\pm</math> 1.1</b> )	59.8 $\pm$ 14.3 ( <b>72.0 <math>\pm</math> 5.2</b> )	68.0 $\pm$ 25.1 ( <b>88.9 <math>\pm</math> 5.3</b> )
0 mV	16.7 $\pm$ 4.0 ( <b>24.8 <math>\pm</math> 0.5</b> )	37.8 $\pm$ 8.2 ( <b>45.2 <math>\pm</math> 1.0</b> )	40.6 $\pm$ 7.0 ( <b>52.8 <math>\pm</math> 10.7</b> )	57.8 $\pm$ 13.0 ( <b>70.4 <math>\pm</math> 1.9</b> )
-200 mV	19.2 $\pm$ 3.7 ( <b>15.0 <math>\pm</math> 0.3</b> )	22.8 $\pm$ 4.6 ( <b>21.8 <math>\pm</math> 0.5</b> )	31.0 $\pm$ 4.7 ( <b>32.4 <math>\pm</math> 1.4</b> )	29.3 $\pm$ 17.0 ( <b>42.0 <math>\pm</math> 2.4</b> )



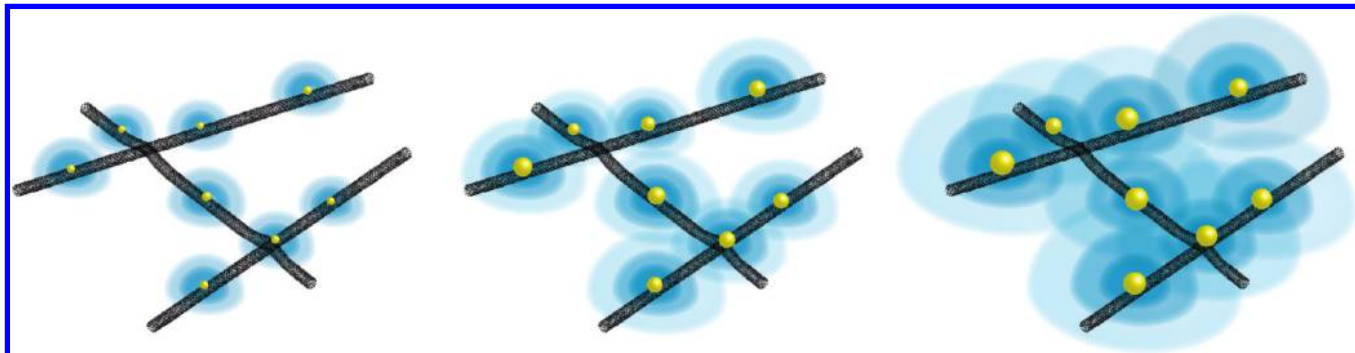


**Figure 7.** Schematic representation showing the three different diffusional time scales which prevail during the nucleation of Au NPs on a SWNT network electrode: (a) short times; (b) intermediate times; (c) long times.

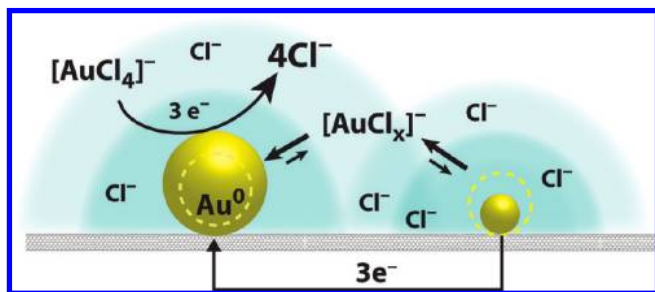


**Figure 8.** Schematic representation of electrochemically induced Ostwald ripening of Au NPs occurring as a result of electron transfer through the conducting SWNT support and via the overlapped diffusion fields, facilitated by equilibria of intermediate  $[\text{AuCl}_x]^-$  complexes and released  $\text{Cl}^-$ .

of  $\text{Cl}^-$  around growing Au clusters (eq 1 and Figure 8);<sup>42,72</sup> an effect more pronounced for closer spaced NPs on the time scale of the experiment.

## Conclusions

We have been able to elucidate the electrodeposition mechanism of Au NPs on two-dimensional SWNT network electrodes under diffusion-limited conditions. Analysis of the chronoamperometric transients in accordance with the Scharifker-Hills nucleation model suggested that nucleation was more “progressive” in nature. However detailed microscopic analysis, using AFM and FE-SEM, of Au NP size and density, as a function of deposition potential and time, indicated that for most deposition potentials and time scales a fixed surface density of NPs prevailed.

The failure of the SH model to predict the nucleation mechanism is attributed to the heterogeneous nature of the electrode substrate employed, where nucleation is highly directional, occurring only on the SWNT network, which covers less than 1% of the insulating surface. It also highlights the need to complement chronoamperometric measurements with high resolution microscopy for study of nucleation on complex electrode surfaces.

An important observation in these studies was that at the highest driving forces and for the longest deposition times the particle density was seen to decrease with time; AFM revealed the presence of both larger and smaller particles on the surface. This was attributed to electrochemically induced Ostwald Ripening, whereby larger particles grow at the expense of smaller ones. Due to the very close nucleated Au NP–Au NP separations at high overpotentials, the underlying SWNTs, which provide a conductive support, high mobility of Au on SWNT sidewalls, and release of  $\text{Cl}^-$  locally upon Au NP nucleation, this process could be seen at fairly short time scales.

**Acknowledgment.** P.V.D. acknowledges financial support from the University of Warwick via the Warwick Postgraduate Research Scholarship (WPRS); P.R.U. and J.V.M. thank the EPSRC for support, EP/H023909. We thank Dr. Ioana Dumitrescu and Dr. Aleix G. Güell for valuable discussions. Part of the equipment used in this research was obtained through Birmingham Science City with support from Advantage West Midlands and the European Regional Development Fund.

**Supporting Information Available:** Typical  $8\ \mu\text{m} \times 12\ \mu\text{m}$  FE-SEM images of electrodeposited Au NPs on the random two-dimensional SWNT network electrode after electrodeposition for 5 s at  $V_{\text{dep}}$  in the range +200 to −200 mV. Images such as these were used to extract particle number densities. This material is available free of charge via the Internet at <http://pubs.acs.org>.

## References and Notes

- (1) Ajayan, P. M. *Chem. Rev.* **1999**, *99*, 1787.
- (2) Dekker, C. *Phys. Today* **1999**, *52*, 22.
- (3) Frank, S.; Poncharal, P.; Wang, Z. L.; Heer, W. A. n. d. *Science* **1998**, *280*, 1744.
- (4) Dumitrescu, I.; Unwin, P. R.; Macpherson, J. V. *Chem. Commun.* **2009**, 6886.
- (5) Wang, J. *Electroanalysis* **2005**, *17*, 7.
- (6) Staii, C.; Johnson, A. T.; Chen, M.; Gelperin, A. *Nano Lett.* **2005**, *5*, 1774.
- (7) Girishkumar, G.; Rettker, M.; Underhile, R.; Binz, D.; Vinodgopal, K.; McGinn, P.; Kamat, P. *Langmuir* **2005**, *21*, 8487.
- (8) Wildgoose, G. G.; Banks, C. E.; Compton, R. G. *Small* **2006**, *21*, 182.
- (9) Walter, E. C.; Murray, B. J.; Favier, F.; Kaltenpoth, G.; Grunze, M.; Penner, R. M. *J. Phys. Chem. B* **2002**, *106*, 11407.
- (10) Deutscher, R. L.; Fletcher, S. *J. Electroanal. Chem.* **1988**, *239*, 17.
- (11) Deutscher, R. L.; Fletcher, S. *J. Chem. Soc., Faraday Trans.* **1998**, *94*, 3527.
- (12) Abyaneh, M. Y. *J. Electroanal. Chem.* **2002**, *530*, 82.
- (13) Abyaneh, M. Y. *J. Electroanal. Chem.* **2002**, *530*, 96.
- (14) Abyaneh, M. Y.; Fleischmann, M. *J. Electroanal. Chem.* **2002**, *530*, 89.
- (15) Day, T. M.; Unwin, P. R.; Wilson, N. R.; Macpherson, J. V. *J. Am. Chem. Soc.* **2005**, *127*, 10647.
- (16) Quinn, B. M.; Dekker, C.; Lemay, S. G. *J. Am. Chem. Soc.* **2005**, *127*, 6146.
- (17) Mirkhalaf, F.; Paprotny, J.; Schiffrin, D. J. *J. Am. Chem. Soc.* **2006**, *128*, 7400.
- (18) Weisbecker, C. S.; Merritt, M. V.; Whitesides, G. M. *Langmuir* **1996**, *12*, 3763.
- (19) Qian, P.; Wu, Z.; Diau, P.; Zhang, G.; Zhang, J.; Liu, Z. *J. Phys. Chem. C* **2008**, *112*, 13346.
- (20) Huang, S.; Qian, Y.; Chen, J.; Cai, Q.; Wan, L.; Wang, S.; Hu, W. *J. Am. Chem. Soc.* **2008**, *130*, 11860.
- (21) Qian, Y.; Huang, S.; Gao, F.; Cai, Q.; Zhang, L.; Hu, W. *J. Phys. Chem. C* **2009**, *113*, 6983.
- (22) Chen, Y.-C.; Young, R. J.; Macpherson, J. V.; Wilson, N. R. *J. Phys. Chem. C* **2007**, *111*, 16167.



- (23) Dumitrescu, I.; Unwin, P. R.; Wilson, N. R.; Macpherson, J. V. *Anal. Chem.* **2008**, *80*, 3598.
- (24) Dumitrescu, I.; Wilson, N. R.; Macpherson, J. V. *J. Phys. Chem. C* **2007**, *111*, 12944.
- (25) Girishkumar, G.; Vinodgopal, K.; Kamat, P. V. *J. Phys. Chem. B* **2004**, *108*, 19960.
- (26) Day, T. M.; Unwin, P. R.; Macpherson, J. V. *Nano Lett.* **2007**, *7*, 51.
- (27) Schlecht, U.; Balasubramanian, K.; Burghard, M.; Kern, K. *Appl. Surf. Sci.* **2007**, *253*, 8394.
- (28) Fan, Y.; Goldsmith, B. R.; Collins, P. G. *Nat. Mater.* **2005**, *4*, 906.
- (29) Faraday, M. *Philos. Trans. R. Soc. London* **1857**, *147*, 145.
- (30) Hutchings, G. J.; Haruta, M. *Appl. Catal., A* **2005**, *291*, 2.
- (31) Tominaga, M.; Shimazoe, T.; Nagashima, M.; Taniguchi, I. *Electrochem. Commun.* **2005**, *7*, 189.
- (32) El-Deab, M. S.; Ohsaka, T. *Electrochem. Commun.* **2002**, *4*, 288.
- (33) Kiyonaga, T.; Akita, T.; Tada, H. *Chem. Commun.* **2009**, 2011.
- (34) Ozel, T.; Gaur, A.; Rogers, J. A.; Shim, M. *Nano Lett.* **2005**, *5*, 905.
- (35) Edgeworth, P. J.; Wilson, N. R.; Macpherson, J. V. *Small* **2007**, *3*, 860.
- (36) Skákalová, V.; Kaiser, A. B.; Woo, Y. S.; Roth, S. *Phys. Rev. B* **2006**, *74*, 085403.
- (37) Bertonecello, P.; Edgeworth, J. P.; Macpherson, J. V.; Unwin, P. R. *J. Am. Chem. Soc.* **2007**, *129*, 10982.
- (38) Macpherson, J. V.; Unwin, P. R. *J. Phys. Chem.* **1995**, *99*, 14824.
- (39) Komsysiaka, L.; Staikov, G. *Electrochim. Acta* **2008**, *54*, 168.
- (40) Martín, H.; Carro, P.; Hernández Creus, A.; González, S.; Salazar, R. C.; Arvia, A. J. *Langmuir* **1997**, *13*, 100.
- (41) El-Deab, M. S.; Sotomura, T.; Ohsaka, T. *J. Electrochem. Soc.* **2005**, *152*, C730.
- (42) Anderson, J. E.; Sawtelle, S. M. *Inorg. Chim. Acta* **1992**, *194*, 171.
- (43) Oesch, U.; Janata, J. *Electrochim. Acta* **1983**, *28*, 1237.
- (44) Oesch, U.; Janata, J. *Electrochim. Acta* **1983**, *28*, 1247.
- (45) Scharifker, B.; Hills, G. *Electrochim. Acta* **1983**, *28*, 879.
- (46) Mirkin, M. V.; Nilov, A. P. *J. Electroanal. Chem.* **1990**, *283*, 35.
- (47) Heerman, L.; Tarallo, A. *J. Electroanal. Chem.* **1999**, *470*, 70.
- (48) Canac, F. C. R. *Chim.* **1933**, *196*, 51.
- (49) Kolmogoroff, A. N. *Bull. Acad. Sci. U.R.R.S. Sci. Mat. Nat.* **1937**, *3*, 355.
- (50) Avrami, M. *J. Chem. Phys.* **1939**, *7*, 1103.
- (51) Avrami, M. *J. Chem. Phys.* **1940**, *8*, 212.
- (52) Avrami, M. *J. Chem. Phys.* **1941**, *9*, 177.
- (53) Johnson, W. A. R. F. M. *Trans. Am. Inst. Min. Metall. Eng.* **1939**, *135*, 416.
- (54) Fletcher, S. *J. Electroanal. Chem.* **2002**, *530*, 105.
- (55) Fletcher, S. *J. Electroanal. Chem.* **2002**, *530*, 119.
- (56) Grujicic, D.; Pesic, B. *Electrochim. Acta* **2002**, *47*, 2901.
- (57) Soto, A. B.; Arce, E. M.; Palomar-Pardavé, M.; González, I. *Electrochim. Acta* **1996**, *41*, 2647.
- (58) Gloaguen, F.; Léger, J. M.; Lamy, C.; Marmann, A.; Stimming, U.; Vogel, R. *Electrochim. Acta* **1999**, *44*, 1805.
- (59) Krumm, R.; Guel, B.; Schmitz, C.; Staikov, G. *Electrochim. Acta* **2000**, *45*, 3255.
- (60) Vinokur, N.; Miller, B.; Avyigal, Y.; Kalish, R. *J. Electrochem. Soc.* **1999**, *146*, 125.
- (61) Schmidt, U.; Donten, M.; Osteryoung, J. G. *J. Electrochem. Soc.* **1997**, *144*, 2013.
- (62) Choi, H. C.; Shim, M.; Bangsaruntip, S.; Dai, H. *J. Am. Chem. Soc.* **2002**, *124*, 9058.
- (63) Guo, J.; Tokimoto, T.; Othman, R.; Unwin, P. R. *Electrochem. Commun.* **2003**, *5*, 1005.
- (64) Dumitrescu, I.; Unwin, P. R.; Macpherson, J. V. *Electrochem. Commun.* **2009**, *11*, 2081.
- (65) Dumitrescu, I.; Dudin, P. V.; Edgeworth, J. P.; Macpherson, J. V.; Unwin, P. R. *J. Phys. Chem. C* **2010**, *114*, 2633.
- (66) Day, T. M.; Wilson, N. R.; Macpherson, J. V. *J. Am. Chem. Soc.* **2004**, *126*, 16724.
- (67) Di Vece, M.; Grandjean, D.; Van Bael, M. J.; Romero, C. P.; Wang, X.; Decoster, S.; Vantomme, A.; Lievens, P. *Phys. Rev. Lett.* **2008**, *100*, 236105.
- (68) Heinemann, K.; Poppa, H. *Thin Solid Films* **1976**, *33*, 237.
- (69) Porter, J. D.; Robinson, T. O. *J. Phys. Chem.* **1993**, *97*, 6696.
- (70) Redmond, P. L.; Hallock, A. J.; Brus, L. E. *Nano Lett.* **2004**, *5*, 131.
- (71) He, Y.; Zhang, J.; Wang, Y.; Yu, Z. *Appl. Phys. Lett.* **2010**, *96*, 063108.
- (72) Goolsby, A. D.; Sawyer, D. T. *Anal. Chem.* **1968**, *40*, 1978.

JP1043706